Imaging carious human dental tissue with optical coherence tomography

A. Z. Freitas,[a] D. M. Zezell, and N. D. Vieira, Jr.
Centro de Lasers e Aplicações, Instituto de Pesquisas Energéticas e Nucleares, Avenida Lineu Prestes, 2242, CEP05422-950, Cidade Universitária "Armando de Salles Oliveira," São Paulo, Brazil

A. C. Ribeiro and A. S. L. Gomes
Departamento de Física, Universidade Federal de Pernambuco, Avenida Professor Luiz Freire, s/n Cidade Universitária, 50670-901 Recife, Pernambuco, Brazil

(Received 2 May 2005; accepted 1 December 2005; published online 23 January 2006)

Optical coherence tomography is an imaging technology that produces high-resolution cross-sectional images of turbid media and internal microstructures including inside living tissue. In this work, three-dimensional images of a dental microstructure, that can be used to make both qualitative and quantitative assessments of oral tissue health, were obtained. It was possible to detect subclinical caries in third molar human teeth, showing that the lesion is located below the surface at 10 μm with a maximum depth lesion of 50 μm. A three-dimensional image was constructed confirming that it is possible to observe different planes inside the sample. It is important to notice that the optical changes induced by the carious disease in dental tissue can be readily detected by the optical coherence tomography method, before structural changes become apparent. © *2006 American Institute of Physics*. [DOI: 10.1063/1.2160716]

I. INTRODUCTION

The application of optical technologies in medicine and biology has a long history. Since the 18th century, the microscope has been an indispensable tool for biologists. With the invention of the laser in 1960, physicians greatly benefitted from less-invasive surgical procedures. The development of fiber optics led to the manufacture of endoscopes, allowing direct view of internal organs deep in the body with minimal invasion. Optical technologies enable easy chemical analysis of tissue samples and the counting and measuring of blood cells. In spite of these and other advances, few of the optical instruments used today in medicine take full advantage of the coherence properties of light.

Optical coherence tomography (OCT) is a diagnostic imaging technology in which the coherence features of photons are exploited, leading to an imaging technology that is capable of producing high-resolution cross-sectional images of the internal microstructure of living tissue. Its applications in medicine were reported less than a decade ago,[1–3] but its roots lie in early works on white-light interferometry, that led to the development of optical coherence-domain reflectometry (OCDR), a one-dimensional (1D) optical ranging technique.[3,4]

Although OCDR was originally developed for finding faults in fiber-optic cables and network components, its capability to probe the human eye structure[5,6] and other biological tissues[7,8] was readily identified. The optical sectioning ability of OCT, due to the short temporal coherence of a broadband light source, enables OCT scanners to image microscopic tissue structures at depths beyond the conventional bright-field and confocal microscopes.

Currently, dentists evaluate the oral health of a patient through three main methods: visual/tactile examination, periodontal probing, and radiographic imaging. Probes are placed between the soft tissue and tooth to assess periodontal conditions. The probe penetration depth is measured and the location of the soft tissue attachment is estimated from a fixed reference point on the tooth. This method can be painful and its diagnostic is imprecise due to variations on insertion force, inflammatory status of tissue, diameter of probe tips, and anatomical tooth contours.[9] Radiographies reveal structural characteristics of teeth and bone that cannot be identified in a visual examination. While radiographies are highly sensitive to detecting regions of significant carious demineralization and bone loss, they have several limitations in identifying periodontal diseases as they provide no information about soft tissue. Also, they are two dimensional and the precise position of a carious lesion is very difficult or even impossible. In addition, radiography uses potentially harmful ionizing radiation and cannot provide information about soft tissue state.

The goal of this work is to use the OCT technique to produce *in vitro* three-dimensional images of a dental microstructure that can be used to make both qualitative and quantitative analyses of dental health. In particular, one expects to identify clinically important anatomical features in particular dental caries.

II. THEORETICAL BASIS OF OCT

Figure 1 shows the basic components of an OCT system. The main part of the system comprehends an interferometer illuminated by a broadband light source.

The OCT system splits the broadband light source beam into a reference field (E_R) and a sample field (E_S). They interfere at the photodetector (PD) by summing up the two electrical fields that are reflected by the optical scanning system (in general a mirror) and the sample. The intensity in the PD can be expressed by[10]

[a]Electronic mails: azanardi@ipen.br and azanardi@gmail.com

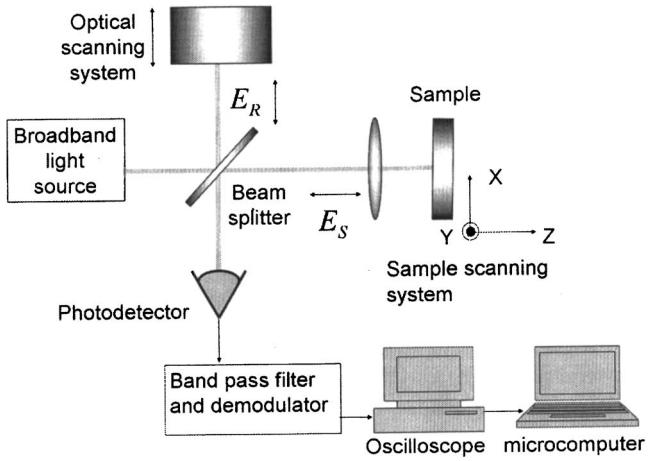

FIG. 1. Critical components of a standard OCT system.

$$I = \left\langle \frac{\eta e}{h\nu} \frac{|E_R + E_S'|}{2\eta_0} \right\rangle. \tag{1}$$

Consider first the monochromatic case, where E is given by

$$E_i = A_i e^{(i\omega t - \beta z)}. \tag{2}$$

Then the intensity [Eq. (1)] becomes

$$I = \frac{e}{h\nu\eta_0}\left(\frac{1}{2}|A_R|^2 + \frac{1}{2}|A_S|^2 + \mathrm{Re}\{E_R E_S'^*\}\right), \tag{3}$$

where the term $\mathrm{Re}\{E_R E_S'^*\} = A_R A_S \cos(2\beta_R l_R - 2\beta_S l_S)$ represents the real part of the interfering term, ω is the optical frequency, and β is the propagation constant (in this case the light source is highly coherent).

For a low-coherence light source with $E_R = A_R(\omega)e^{-i[2\beta_R(\omega)l_R - \omega t]}$ and $E_S' = A_S(\omega)e^{-i[2\beta_S(\omega)l_S - \omega t]}$, where $A_R(\omega)$ and $A_S(\omega)$ are the amplitudes and $\beta_i(\omega)$ the propagation constants for broadband light source, the intensity on the photodetector is

$$I = \frac{e}{h\nu\eta_0}\mathrm{Re}\left\{\int_{-\infty}^{\infty}\left(\underbrace{\frac{1}{2}|A_R(\omega)|^2 + \frac{1}{2}|A_S(\omega)|^2}_{\text{dc component}} + \underbrace{S(\omega)e^{-\Delta\phi(\omega)}}_{\text{ac component}}\right)\frac{d\omega}{2\pi}\right\}, \tag{4}$$

where $S(\omega)$ and $\Delta\phi(\omega)$ are defined as $S(\omega) = A_S(\omega)A_R(\omega)^*$ and $\Delta\phi(\omega) = 2[\beta_S(\omega)l_S - \beta_R(\omega)l_R]$; the first term on the right-hand side is identified as the dc component while the second term is the ac component, which is experimentally detected.

Considering the case where the sample and the reference arms consist of a uniform, linear, nondispersive material and the light source spectral density is given by $S(\omega - \omega_0)$, which is considered to be bandwidth limited and centered at the frequency ω_0. The propagation constants $\beta_i(\omega)$ in each arm are assumed to be the same; the diffuse tissue material behaves locally as an ideal mirror leaving the sample beam unchanged. Propagating the $\beta_i(\omega)$ coefficient as a first-order Taylor expansion around the central frequency ω_0 gives

$$\beta_R(\omega) = \beta_S(\omega) = \beta(\omega_0) + \beta'(\omega_0)(\omega - \omega_0). \tag{5}$$

Then the phase mismatch $\Delta\phi(\omega)$ is determined solely by the length mismatch $\Delta l = l_S - l_R$ between the reference and the sample arms, and is given by

$$\Delta\phi(\omega) = \beta(\omega_0)(2\Delta l) + \beta'(\omega_0)(\omega - \omega_0)(2\Delta l). \tag{6}$$

Now, consider that the light source has a Gaussian power spectral density defined by

$$S(\omega - \omega_0) = \sqrt{\frac{2\pi}{\sigma_\omega^2}} e^{-(\omega - \omega_0)^2/\sigma_\omega^2}, \tag{7}$$

which has been normalized to the unit power, $\int_{-\infty}^{\infty} S(\omega)d\omega/2\pi = 1$, where $2\sigma_\omega$ is the standard deviation of the power spectral bandwidth. Using this power spectrum [Eq. (7)] and the phase mismatch [Eq. (6)] into Eq. (4) one obtains the photodetector signal V,

$$V = \frac{\eta e}{h\beta\eta_0}\mathrm{Re}\{1 + e^{-\Delta\tau_g^2/2\sigma_\tau} e^{-i\omega_0\Delta\tau_p}\}. \tag{8}$$

In Eq. (8), the phase delay mismatch $\Delta\tau_p$ and the group delay mismatch $\Delta\tau_g$ are defined as

$$\Delta\tau_p = \frac{\beta(\omega_0)}{\omega_0}(2\Delta l) = \frac{2\Delta l}{v_p}, \tag{9}$$

and

$$\Delta\tau_g = \beta'(\omega_0)(2\Delta l) = \frac{2\Delta l}{v_g}. \tag{10}$$

The photodetector signal given by Eq. (8) contains two terms, the first one is the mean (dc) intensities returning from the reference and sample arms of the interferometer, and the second one, which depends on the optical time delay set by the position of the reference mirror, represents the amplitude of the interference fringes that carry information about the tissue structure, this is a Gaussian envelope with a characteristic standard deviation temporal width $2\sigma_\tau$, that is inversely proportional to the power spectral bandwidth: $2\sigma_\tau = 2/\sigma_\omega$. This envelope falls off quickly with increasing group delay mismatch $\Delta\tau_g$ and is modulated by interference fringes that oscillate with increasing phase delay mismatch $\Delta\tau_p$. Thus, the second term in Eq. (8) defines the axial resolving power of the OCT system. For a Gaussian shape function with standard deviation σ, the full width at half maximum (FWHM) is $2\sigma\sqrt{2\ln 2}$ then, the axial resolution of the system is

$$\Delta l_{\mathrm{FWHM}} = \frac{2\ln 2}{\pi}\frac{\lambda_0^2}{\Delta\lambda}, \tag{11}$$

where λ_0 is the center wavelength.

The optical scanning system consists of a grating-lens pair in a folded, double-pass, Fourier frequency-domain pulse shaping configuration,[11] as shown in Fig. 2 and depicted in a three-dimensional (3D) view in Fig. 3 (inset). A flat mirror in a scanning galvanometer serves as a spatial phase filter which imposes a linear phase ramp in the frequency domain. The delay line is based on the well-known

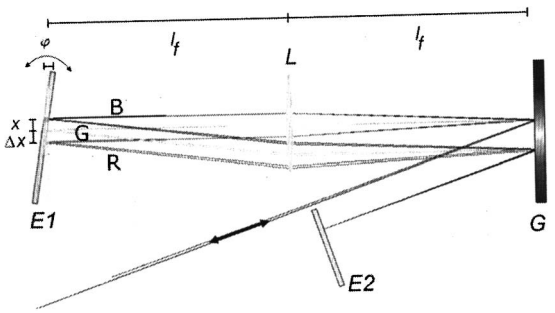

FIG. 2. Fast Fourier scanning as an optical delay line. The beam is diffracted by the diffraction grating (G), collimated by lens (L), reflected in the galvanometer mirror (E1) returned to the lens, recomposed in the grating, reflected by the folding mirror and retroreflected through the grating, lens, galvanometer mirror, lens, and finally recomposed in the grating, returning in the same incoming way.

property of the Fourier transform: A phase ramp in the frequency domain corresponds to a group delay in the time domain.

$$x(t-t_0) \overset{\mathfrak{T}}{\leftrightarrow} X(\omega)e^{-i\omega t_0}. \tag{12}$$

The angle of the incident beam on the grating was selected such that the center wavelength λ_0 of the diffracted beam was normal to the grating (G) and the entire grating was in the focal plane of the lens (L). This was done in order to prevent the introduction of group-velocity dispersion (GVD) which varied through the course of a scan. If the grating is at an angle not normal to the optical axis of the lens, then as light is laterally displaced on the grating by the scanning mirror, it is also displaced from the focal plane of the lens, introducing GVD.[11,12]

The mirror pivot (E_1) can be offset from the center wavelength by an arbitrary distance x obtained by a simple translation of the scanning mirror. The phase shift $\phi(\lambda)$ as a function of the wavelength λ for a given mirror tilt angle φ may be written as (see Fig. 2)

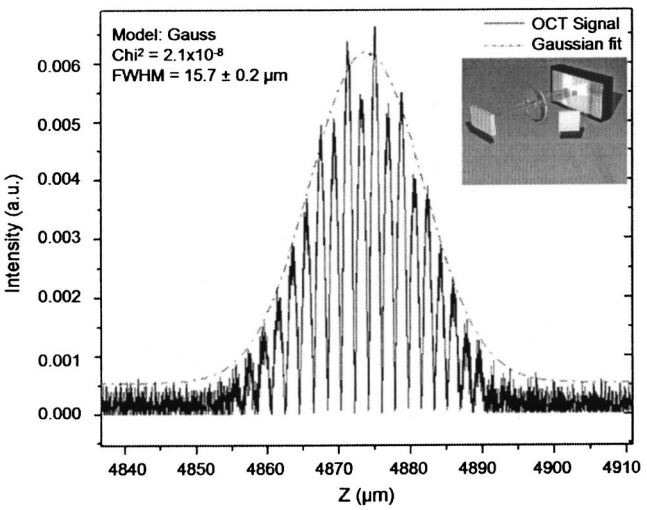

FIG. 3. OCT signal, used for calibration, obtained with a mirror as the sample. The inset shows a view of the optical delay line. The beam is diffracted by the grating and collimated by the lens in the scanning mirror.

$$\phi(\lambda) = \frac{8\pi\varphi x}{\lambda} + \frac{8\pi\varphi l_f(\lambda-\lambda_0)}{p\lambda\cos\theta}, \tag{13}$$

where l_f is the focal length of the lens and p is the pitch of the grating lines. This function was derived using the grating equation $n\lambda = p(\sin\theta_i + \sin\theta)$, where n is the diffraction order ($n=1$ in our case), θ_i is the grating incident angle (0°), and θ is the grating refraction angle and assuming that the small-angle approximation $\sin(\theta) \cong \theta$ holds for the diffraction angles within the bandwidth. The distance Δy that a wavelength component λ traverses as a function of the scanning mirror tilt angle σ is calculated (taking into account the fact that the beam traverses the path Δy four times) and multiplied by $2\pi/\lambda$ to convert from displacement into phase shift. This phase shift can also be written as a function of the angular optical frequency ω,

$$\phi(\omega) = \frac{4\sigma x\omega}{c} - \frac{8\pi\sigma l_f(\omega-\omega_0)}{p\omega}, \tag{14}$$

where ω_0 is the center angular optical frequency. From Eq. (14) and the definition of group delay,

$$t_g = \left.\frac{\delta\phi(\omega)}{\delta\omega}\right|_{\omega=\omega_0} = \frac{4\sigma x}{c} - \frac{4\sigma l_f\lambda_0}{cp}, \tag{15}$$

this corresponds to the free space-group path-length difference Δl_g,

$$\Delta l_g = 4\sigma x - \frac{4\sigma l_f\lambda_0}{p}. \tag{16}$$

In the above equation [Eq. (16)], for a given set of parameter, the pitch grating lines (p), the mirror tilt angle (σ), the focal length lens (l_f), and the central wavelength (λ_0) can be used to determine the total path length. In this configuration a small tilt angle produces a large scan path-length difference. The second term is dominant in our configuration, and the x value can be adjusted for the central wavelength (Fig. 2).

III. MATERIALS AND METHODS

The configuration employed in the OCT system was the "open air" Michelson interferometer illustrated in Fig. 1. In this type of interferometer, light from the source propagates through a 50/50 beam splitter, where half of the optical intensity is transmitted to the delay line. The remaining half of the light is directed to the sample. The light source was a mode-locked Ti:sapphire laser (Mira-Coherent) centered around 830 nm with 51 fs pulse width and 20 nm FWHM spectral width. The autocorrelation trace (Fig. 4) was measured with an autocorrelator (homemade), and in Fig. 5 the spectral distribution was measured with a fast spectrometer [positive light, ULS model 97188F]. The laser system provided an average power 100 mW (Ophir PowerMeter) at a repetition rate of 76 MHz. The delay line was implemented with a scanner (general scanning 6120D) operating at a frequency of 200 Hz, a grating with 590 lines/mm ($p = 1.69$ μm), 25×25 mm^2 lateral dimensions, and a lens with 50 mm of focal length. The maximum angular excursion of the scanning mirror was set to $\varphi = 2°$ to produce a usable group delay scan of approximately $\Delta l_g = 2.7$ mm. A low noise

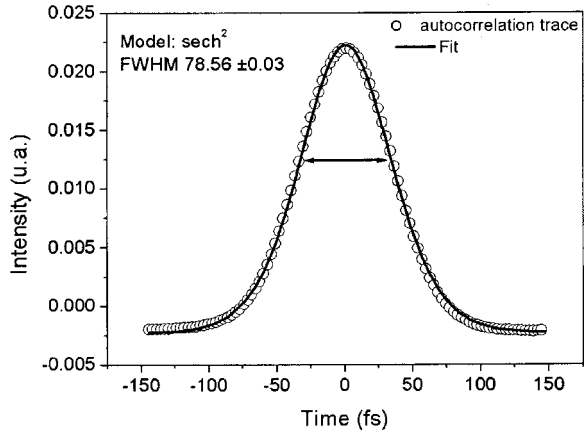

FIG. 4. Autocorrelation trace for laser pulse. The pulse width was determined simply dividing the autocorrelation width by 1.54, given the pulse width of 51 fs.

amplified detector (SR-194) with an electronic circuit detecting only the positive part of the signal, as shown in Fig. 3, was used. A digital oscilloscope was employed to display the data (Tektronix 3000B) and subsequently stored onto a personal computer. To displace the sample in the x axis, in order to obtain an image, we use a computer-controlled translation stage (Thorlabs, T25-XYZ) with a minimum step of 0.05 μm.

The samples studied were human third molar teeth with artificial caries lesion created on the buccal surface. This surface was coated with an acid-resistant varnish, except for a 2 mm square window. The pH demineralization and remineralization cycling model[13] was used to produce the artificial lesions. This cycle was repeated for 9 days, then the teeth were kept in a remineralizing solution for 2 days before the varnish was removed. The teeth were rinsed with double-de-ionized water and stored in a humid environment.

IV. RESULTS

Figure 3 shows the axial resolution of the system obtained with a mirror in the position of the sample. The width of Gaussian fit was 15.7(0.2) μm FWHM.

The laser beam was focused into the sample with a 50 mm focal length lens, providing a lateral resolution of 10 μm, calculated using $\Delta x=(4\lambda_0/\pi)(f/d)$ where f is the lens' focal length, d is the beam waist, and λ_0 is the laser central wavelength. The images were produced with a lateral and axial scan step of 15 μm. Figure 6 shows the result for one scan in the health region of the tooth after the varnish was removed. The raw data was smoothed by fast Fourier transform (FFT) filtering. The smoothing was accomplished by removing Fourier components with frequencies higher than $(1/n\Delta t)$, where n is the number of data points considered at a time, and Δt is the spacing between two adjacent data points. The function used to filter out the high-frequency components was a parabola with its maximum of 1 at zero frequency and falling to zero at the cutoff frequency defined above.[14] In our case, one complete axial scan with 10 000 points corresponds to 2730 μm, so we used 55 points for smoothing corresponding to our resolution of 15 μm. One can see two main peaks, dividing the region into three parts. The first one, in light gray, corresponds to the air, between the two peaks in gray, it is the enamel, and after the second one, in dark gray, it is the dentine.

The OCT signal from the region where the lesion was produced is shown in Fig. 7, where different behaviors can be seen, when compared to the healthy region (Fig. 6). Close to the first peak in the OCT signal, there is a second structure, corresponding to the back surface of the lesion region.

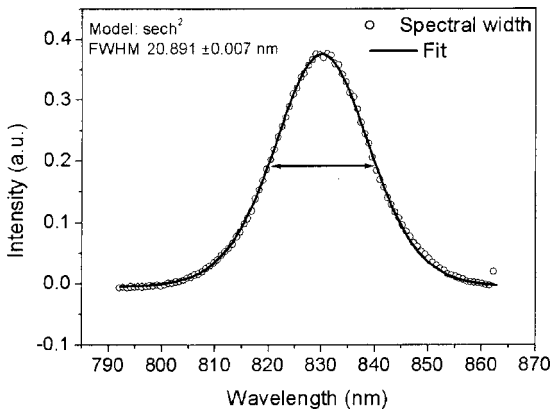

FIG. 5. Spectrum of Ti:sapphire laser (Mira) centered around 830 nm.

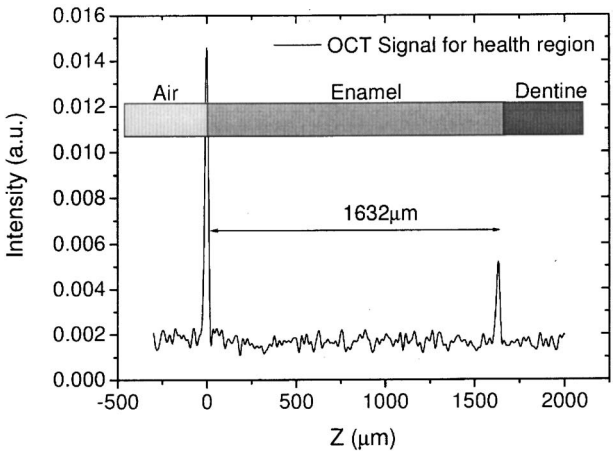

FIG. 6. OCT signal from a healthy region of the tooth; the light gray part in the picture is signal from the air; the gray represents the enamel and the dark gray part is the dentine of the tooth.

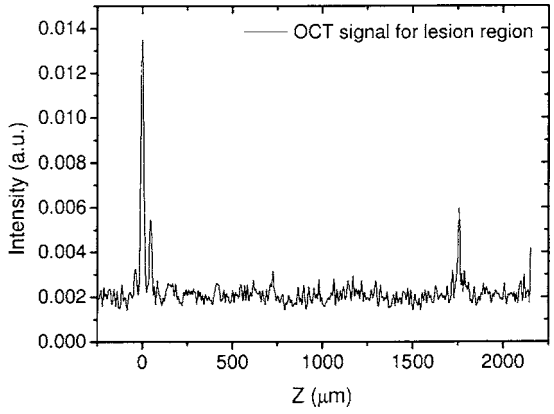

FIG. 7. OCT signal from a region with a caries lesion; the second peak is the back surface of the lesion.

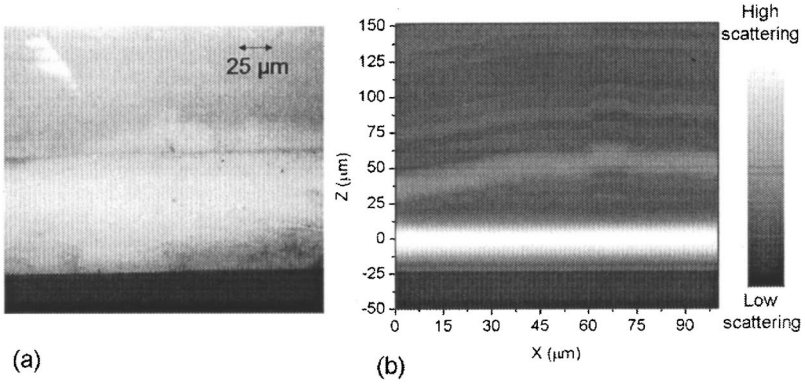

FIG. 8. (a) Optical microscope image of region lesion and (b) OCT image constructed by scans in different lateral positions of the sample.

The distance between the first peak, interface air/enamel, and the second one, enamel/lesion depends on the lesion structure. In the case shown in Fig. 7, it was 40 μm, whereas in other regions the total range varied from 20 up to 50 μm.

Figure 8(a) shows the optical microscope image (Leika DMLP), using polarized light, obtained after cutting the sample in the lesion region, where observation by OCT scan was performed.

The OCT cross-section image, Fig. 8(b), was constructed using the depth-priority scanning protocol (A scan), where axial scans are acquired at successive transverse positions. The tooth was moved laterally, perpendicular to the laser axis, in 10 μm increments. All scans were normalized to a maximum OCT signal (front surface) and a false-color gray scale was used.

To obtain the results shown in Fig. 9(d), transverse image sections from different positions of the sample in the *y* axis (Fig. 1) were grouped. The construction was accomplished with the aid of an analysis software and voxel visualization (VGSTUDIO Max 1.2). This three-dimensional reconstruction allows a transversal sections analysis different from those obtained directly from the OCT system. In the sequence shown in the illustration of Fig. 9, the subtraction of the carious tissue, whose selection was based on raw signal from the OCT data, applied a threshold on color map and selected a resultant region by color similarity.

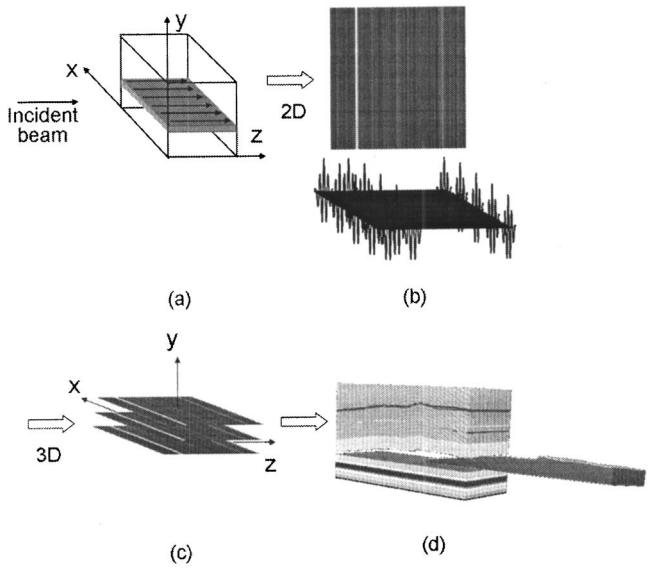

FIG. 9. Principle of OCT image construction: single scan (a), bidimensional image (b), three-dimensional image construction (c), and tomographic construction of lesion region of the tooth (d).

V. DISCUSSION

In this work an OCT system with a fast Fourier scan delay line was implemented, showing that it is possible to image internal structure of dental tissue. In particular, it was shown that it is possible to detect early artificial caries. Figure 6 shows the structure of a healthy region of one tooth, where the distance between the interface enamel/dentine and the tooth surface was measured to be 1632(15) μm, corrected by refraction index of tooth[15] (1.62 at 856 nm), which is in agreement with the optical microscope image, demonstrating the linearity of the scan delay line. In Fig. 7, it is possible to see the demineralization induced by acid attack, evinced by the appearance of an adjacent small peak. The cross-section image, Fig. 8(b), clearly shows the demineralization process taking place in the tooth. It is possible, in principle, to measure the reflectivity variation of the interfaces, as it was done in the work by Amaechi *et al.*.[16] The OCT system, in the near future, will provide a powerful contactless and noninvasive diagnostic method and could be used to replace, or complement, the traditional diagnostic methods such as x-ray radiography, avoiding potentially hazardous ionization radiation and enabling 3D images to be generated.

It is important to emphasize that the optical changes in carious tissue can be readily detected by the OCT, before structural changes become apparent by conventional detection methods.

ACKNOWLEDGMENTS

We gratefully acknowledge the technical contribution of Dr. John Girkin from the Institute of Photonics, University of Strathclyde, Glasgow-Scotland-UK, and Dr. Martha Marques Ferreira Vieira for language revision. This research was supported by FAPESP (Grant No. 00/15135-9) and CAPES/PROCAD (Grant No. 0156/01-9).

[1] J. G. Fujimoto, M. E. Brezinski, G. J. Tearney, S. A. Boppart, B. E. Bouma, M. R. Hee, J. F. Southern, and E. A. Swanson, Nat. Med. **1**, 970 (1995).
[2] A. F. Fercher, C. K. Hitzenberger, W. Drexler, G. Kamp, and H. Sattmann, Am. J. Ophthalmol. **116**, 113 (1993).

[3]R. C. Youngquist, S. Carr, and D. E. N. Davies, Opt. Lett. **12**, 158 (1987).
[4]K. Takada, I. Yokohama, K. Chida, and J. Noda, Appl. Opt. **26**, 1603 (1987).
[5]A. F. Fercher, K. Mengedoht, and W. Werner, Opt. Lett. **13**, 1867 (1988).
[6]J. A. Izatt, M. R. Hee, E. A. Swanson, C. P. Lin, D. Huang, J. S. Schuman, C. A. Puliafito, and J. G. Fujimoto, Arch. Ophthalmol. (Chicago) **112**, 1584 (1994).
[7]W. Clivaz, F. Marquis-Weible, R. P. Salathe, R. P. Novak, and H. H. Gilgen, Opt. Lett. **17**, 4 (1992).
[8]J. M. Schmitt, A. Knüttel, and R. F. Bonner, Appl. Opt. **32**, 6032 (1993).
[9]L. Mayfield, G. Bratthall, and R. Attstrom, J. Clin. Periodontol. **23**, 76 (1996).
[10]M. R. Hee, *Handbook of Optical Coherence Tomography*, edited by Brett E. Bouma, 1st ed. (Marcel Dekker, New York, 2001), Chap. 2, pp. 41–66.
[11]G. J. Tearney, B. E. Bouma, and J. G. Fujimoto, Opt. Lett. **22**, 1811 (1997).
[12]O. E. Martinez, IEEE J. Quantum Electron. **QE-23**, 59 (1987).
[13]J. D. Featherstone, N. A. Barrett-Vespone, D. Fried, Z. Kantorowitz, and W. Seka, J. Dent. Res. **77**, 1397 (1998).
[14]Computer program ORIGIN6.0, SR4 (Microcal Software Inc, Northampton, MA, 1991–2000).
[15]X. J. Wang, T. E. Milner, J. F. de Boer, Y. Zhang, D. H. Pashley, and J. Stuart Nelson, Appl. Opt. **38**, 2092 (1999).
[16]B. T. Amaech, A. Gh. Podoleanu, G. N. Komarov, J. A. Rogers, S. M. Higham, and D. A. Jackson, Laser Phys. **13**, 703 (2003).